Controlled spherical deuterium droplets as Lagrangian tracers for cryogenic turbulence experiments

Clément Bret, Jérôme Chartier, Pantxo Diribarne, Jérôme Duplat, Bernard Rousset

Controlled spherical deuterium droplets as lagrangian tracers for cryogenic turbulence experiments

Clément Bret,[1] Jérôme Chartier,[1] Pantxo Diribarne,[1] Jérôme Duplat,[1] and Bernard Rousset[1]
dSBT/IRIG CEA, Université Grenoble Alpes - F-38054 Grenoble, France

(*Electronic mail: pantxo.diribarne@univ-grenoble-alpes.fr)

(Dated: 2 October 2023)

The study of the smallest scales of turbulence by (lagrangian) particle tracking faces two major challenges: the requirement of a 2D or 3D optical imaging systems with sufficiently high spatial and temporal resolution, and the need for particles that behave as passive tracers when seeded into the flow. While recent advances in the past decade have led to the development of fast cameras, there is still a lack of suitable methods to seed cryogenic liquid helium flows with mono-disperse particles of sufficiently small size, of the order of a few micrometers, and a density close enough to that of helium. Taking advantage of the surface tension, we propose two different techniques to generate controlled liquid spherical droplet of deuterium over a liquid helium bath. The first technique operates in a continuous mode by fragmenting a liquid jet thanks to the Rayleigh-Taylor instability. This results in the formation of droplets with a diameter distribution of $2 \pm 0.25 D_N$ where D_N is the diameter of the jet nozzle ($D_N = 20\,\mu$m in the present experiment). This method offers a high production rate, greater than 30 kHz. The second technique operates in a drop-on-demand mode by detaching droplets from the nozzle using pressure pulses generated by a piezoelectric transducer. This approach yields a much narrower diameter distribution of $2.1 \pm 0.05 D_N$ but at a smaller production rate, in the range 500 Hz-2 kHz. The initial trajectories and shapes of the droplets, from the moment they are released from the nozzle until they falls 3 mm below, are investigated and discussed based on back-light illumination images.

I. INTRODUCTION

Liquid helium has attracted much interest for the study of hydrodynamics mainly due to its potential to produce highly turbulent flows in laboratory size experiments. In its normal state, He I, liquid ^{4}He has a kinematic viscosity of the order of $2 \times 10^{-8}\,\mathrm{m^2/s}$, i.e. almost fifty times lower than that of water at room temperature. The range of accessible turbulent Reynolds numbers Re is typically 10^2-10^5 in apparatus of size 1 mm to 1 m. The counterpart is that in order to study the structure of turbulence down to dissipative Kolmogorov length scales η, measurement instruments must have spacial resolutions of the order of 50 µm or below, even in large experiments[1].

In the superfluid state, He II, the proper definition of dissipative scale is subject to debate. He II can be seen as an intimate mixture of two components[2,3]: the normal component behaves like a classical viscous fluid and carries all the enthropy of the flow, while the superfluid component is inviscid and carries no enthropy. The proportion of normal component goes from 100% at $T_\lambda = 2.17\,$K down to 0% at 0 K. One of the consequences is that vorticity in the superfluid component must be concentrated in thin atomic size filaments with a quantized circulation $\kappa \approx 10^{-7}\mathrm{m^2/s}$. At high temperature they act as defects onto which the normal fluid excitations are scattered and share their momentum with the superfluid component. At low temperature vortex reconnections are thought to be the main mechanism by which mechanical energy is dissipated. In He II, in addition to the Kolmogorov length scale, the mean vortex spacing δ is thus also a relevant scale when it comes to dealing with dissipation. In coflow homogeneous and isotropic turbulence, which is forced mechanically at large scale like in classical turbulence, Babuin *et al.*[4] have shown that δ behaves like the Kolmogorov length scale, i.e., $\delta \propto Re^{-3/4}$, and it is thus expected to be of the same order of magnitude (see also estimations of η and δ in a towed grid experiment in Ref. [5]), i.e. a few tens of micrometers. On the other hand, in counter-flow turbulence (see, e.g., Tough[6]), which is forced thermally and has no classical counterpart, the inter-vortex distance depends on the inverse of the applied heat flux and also reaches values of the orders of a few tens of microns in state of the art experiments[7,8].

Despite recent progress, conventional Eulerian velocity sensors such as hotwires, Pitot or micro cantilever anemometers[1,9–12], or He II specific vortex line density sensors[13] still do not permit reliable measurements at such small spatial scales. On the other hand, solid particle based Lagrangian measurements look like a promising candidate for accessing small scales and those techniques have attracted much more interest. Historically experimentalists have resorted to solidified gas flakes (H_2, D_2, $H-D$, Ne, N_2), polymers, or hollow glass micro-spheres. Some counter-flow experiments in He II have shown that the interpretation of particle trajectories may be tricky though: when the two components are forced to flow in opposite directions, those experiments show that the distribution of particle velocities is bimodal, with part of the particles moving at the same velocity as the normal component, and part of them moving at an intermediate velocity between the two components (see Refs. [14–16]). This experimental observation is attributed to the trapping of some of the particles in the vortex tangle (see, e.g. Refs. 17 and 18) that is generated in the turbulent counterflow. A number of theoretical and numerical efforts have been devoted to this puzzling phenomenon and more generally to the vortex-particle interaction (see, e.g., Refs. [19 and 20] and references therein) all of which postulate spherical symmetry for the particles. This condition is never met in practice since most experiments nowadays use frozen hydrogen or deuterium flakes. Careful experimental work is needed to de-

cide to what extent theoretical and numerical results are applicable to real life experiments and build a proper framework for the interpretation of particle trajectories at scales close to the inter vortex spacing. In particular understanding which geometrical parameters influence the trapping of particles, would be helpful in determining to which velocity fields a particle is attached to depending on the underlying flow forcing[21].

In this article we describe two different techniques to produce spherical particles with controlled diameter. The principle is to inject spherical liquid droplets in gaseous helium and let them freeze as they approach the helium free surface below. The droplet production is obtained either using the fragmentation of a liquid jet through the Rayleigh-Plateau instability or using a drop-on-demand piezo assisted device. Those techniques can be applied to any liquid with a density higher or equal to that of helium, and we chose D_2 for this first proof of concept.

After a short review of available techniques to obtain spherical particles, we describe our experimental setup and our first results.

II. AVAILABLE SPHERICAL PARTICLES AT CRYOGENIC TEMPERATURE

Zhang *et al.* [22] have written an extensive review of available solid particles at cryogenic temperatures and, even though it dates back 20 years, references therein are still relevant (except maybe the available manufacturers which may have disappeared or discontinued production for some particle types).

Commercially available solid tracers have been used successfully[23–25], but the density of the particles (even hollow ones) is always higher than that of liquid helium for diameters less than a few tens of micrometers. Other attempts have been made using more exotic particles, e.g., electrons[26,27] or fluorescent nanoparticles[28]. Unfortunately, the former involves intense sound waves[29] affecting the local velocity, and the latter, due to the low efficiency of fluorescence, requires very long exposure times and/or high lightning power density (of order 30 ms for $20\,\mathrm{kW/m^2}$). Excimer[30] are another exotic kind of particles that have shown to be useful at tracking e.g. the spreading of fluid particles initially aligned, but those kind of particles are inappropriate for individual tracking, and for the analysis of the statistics of, e.g., particle acceleration or separation in time.

Injection of mixtures of various gases (Ne, Air, N2, H2, D_2...) highly diluted in helium gas is now the most common way for producing particles for tracking in cryogenic helium. These H_2 or D_2 flakes are neither spherical nor monodisperse in size though.

Çelik *et al.* [24] tried to inject liquid $H_2 - D_2$ mixtures in liquid and take advantage of the surface tension to produce spherical liquid droplets in the gaseous helium sky above a liquid helium bath. The apparatus consisted of a drop-on-demand device with a 1 mm diameter orifice assisted by a mechanical oscillator. Unfortunately, the large orifice size used at the time did not allow the spherical shape or the initial droplet of to be maintained until the droplet froze. They also tried to produce neon droplets in atomization regime[31], but the resulting range of droplets diameters was quite large.

In the community of particle physics, there is also a need for small spherical solid targets to study laser interactions or collisions with exotic ions. Two main teams contributed the development of spherical solid particles injectors in vacuum based on the Rayleigh Plateau instability[32–34], assisted by a vibrating piezoelectric transducer. The main difference between their respective approaches resides in the way they cope with the necessity of letting the pressure surrounding the droplets decrease from the triple point pressure to vacuum.

In this article, we present two solutions dedicated to the injection of D_2 droplets above a liquid helium bath using two techniques. The first, similar to Refs. [32 and 34], is based on the Rayleigh Plateau instability and is suitable for producing large amounts of seeding particles, while the the second is a drop-on-demand mode with better control on the diameter distribution but smaller particle production rate.

III. EXPERIMENTAL SETUP

We describe in the following two subsections the apparatus and the deuterium injection procedure.

A. Apparatus

The experiment was carried out in the OGRES cryostat[25] which was entirely redesigned for better optical accuracy and thermal efficiency (see Fig. 1a) Schematic of the OGRES cryostat. b) Details of the deuterium injection systemfigure.1).

The cryostat is made of two stainless steel vessels equipped with flat visualization windows. In the interstitial space between the two vessels, the pressure is kept below 1×10^{-6} mbar and a thermal copper shield is maintained at $T_{\mathrm{screen}} \approx 100\,\mathrm{K}$ by a controlled flow of liquid nitrogen, in order to prevent heat losses.

The deuterium injection system is made of three successive parts: (i) the gas injection tank and associated valves at room temperature, (ii) the liquid reservoir and (iii) the droplet production nozzle at low temperature. The latter are inside the cryostat, suspended above the liquid helium bath with which they are thermally linked through a copper wire.

The liquid deuterium reservoir is where the condensation of gas deuterium happens. It is made of a cylindrical copper part, 3 cm in diameter and 4 cm in height, in which are drilled 16 parallel channels 3 mm in diameter, leading to a $3.4\,\mathrm{cm}^3$ internal volume. This geometry has been chosen to maximize the heat exchange surface between the copper and the gas deuterium and thus enhance the D_2 condensation rate.

The injection nozzle is a Microfab® MJ-SF-02-20, with a nozzle diameter $D_N = 20\,\mu\mathrm{m}$, plugged below the reservoir through a 5 µm porous filter attached to the VCR fitting seal.

Both the liquid reservoir and the nozzle are equipped with a $100\,\Omega$ heater resistor and a pre-calibrated Cernox® thermometer. Their temperature can thus be controlled independently. Since, in normal conditions, the deuterium inside the reservoir

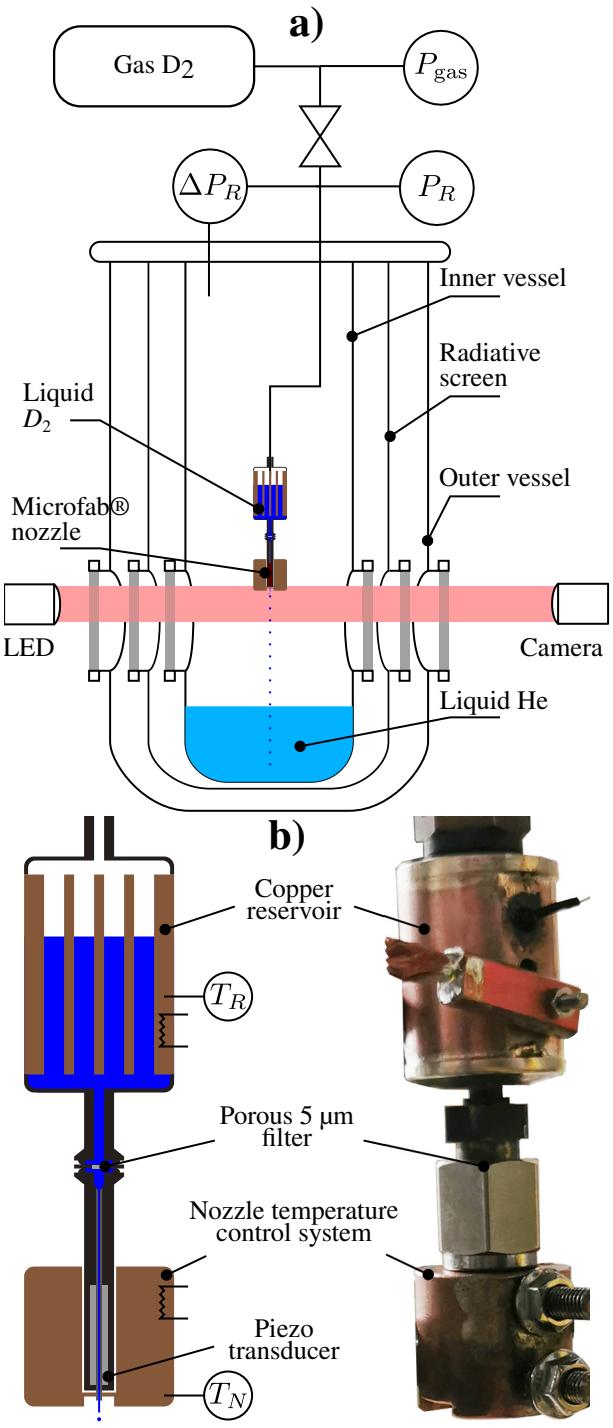

FIG. 1. a) Schematic of the OGRES cryostat. b) Details of the deuterium injection system.

is at saturation pressure, we can also use the absolute pressure of the reservoir, or the pressure difference ΔP_R between the cryostat and the reservoir as an input for the control system, allowing for fine tuning of the liquid ejection velocity.

The visualization system consists in a Photron® Fastcam SA5 camera, with a cropped field of view of 1016×64 pixels, operated at frame rates in the range 30-150 kHz, and

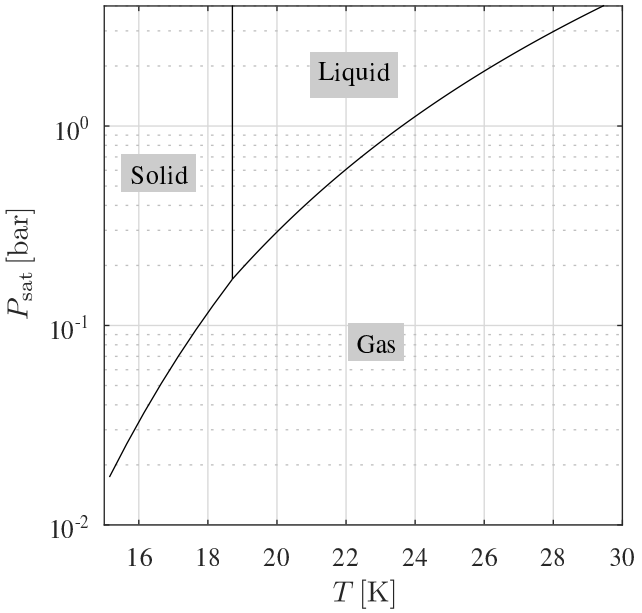

FIG. 2. Phase diagram of deuterium. Liquid-gas saturation pressures data are obtained using the CoolProp library[35]. Solid-liquid and solid-gas saturation pressures are obtained from Gas Encyclopedia.

a Thorlabs® collimated red LED M625L2-C4 for the light source. The camera is fitted with a Questar® QM 100 long distance microscope leading to a spatial resolution of about 4.6 µm/pixel.

B. Injection procedure

Two techniques are used to produce spherical droplets: the Rayleigh-Plateau jet fragmentation and piezo-assisted drop-on-demand.

In both cases the procedure to prepare liquid deuterium and tune the pressure difference is the same. First the reservoir, which is initially filled with gas helium, has to be sealed in order to allow the condensation of liquid deuterium. The temperature of the reservoir is maintained at $T_R \approx 22$ K, i.e. above the triple point of deuterium ($T \approx 18.7$ K, see Fig. 2Phase diagram of deuterium. Liquid-gas saturation pressures data are obtained using the CoolProp library[35]. Solid-liquid and solid-gas saturation pressures are obtained from Gas Encyclopediafigure.2), while the nozzle temperature is kept below, at $T_N \approx 15$ K. Then the injection valve, connecting the deuterium gas tank, at room temperature and $P_{gas} \approx 1.5$ bar, to the reservoir at low temperature, is open in order to let the deuterium in. After a few seconds, the pressure in the reservoir P_R starts to rise until it reaches $P_R = P_{gas}$, indicating that the nozzle has been sealed by a plug of frozen deuterium.

The reservoir is then filled with liquid deuterium by successively, opening the valve a few seconds, and closing it. Unless the reservoir is full, after closing the valve the pressure de-

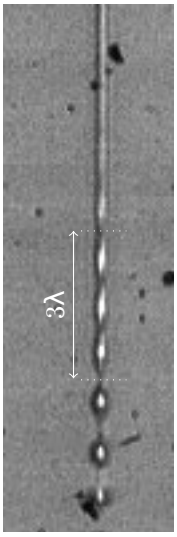

FIG. 3. Destabilization and fragmentation of the deuterium jet

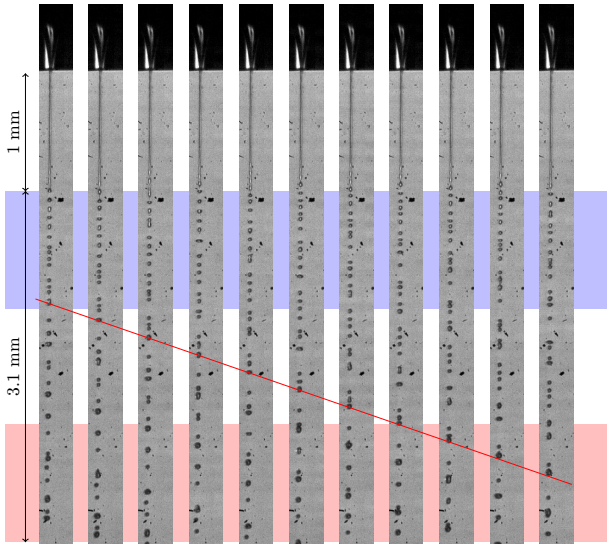

FIG. 4. Snapshots of the deuterium jet and droplets. From left to right, frames are separated by 33.3 μs. The red line indicates the trajectory of one single droplet and allows for measuring the droplet and jet velocity ($v_J \approx 4.4\,\mathrm{m/s}$). The blue area indicates the region near the breakup. The red area indicates the furthest region.

creases down to the saturation pressure at 22 K ($P_{\mathrm{sat}} \approx 0.7$ bar) in a few tens of seconds. We reiterate this operation until the pressure in the reservoir stops decreasing, which indicates that the reservoir is full of liquid at which point we are ready to produce D_2 droplets.

At this point, in order to let the liquid deuterium flow out, the frozen deuterium plug is melt down by increasing the nozzle temperature above the triple point, usually $T_N \approx 21$ K.

IV. DROPLET PRODUCTION

In this section we describe the droplets produced after breakup of a continuous jet and with piezo-assisted drop-on-demand technique.

A. Continuous jet

Downstream of the nozzle, a cylindrical jet of liquid deuterium is formed in an atmosphere of gas helium. The diameter D_J of the jet is indistinguishable from the nozzle diameter D_N. This jet progressively destabilizes in a varicose mode of which the wavelength λ is estimated to be of the order of $\lambda \approx 4-5D_N$ (see Fig. 3Destabilization and fragmentation of the deuterium jetfigure.3). Finally the jet breaks up into droplets, typically at a distance of 1 mm ($\approx 50D_N$) from the nozzle.

These droplets have a rectilinear trajectory at constant velocity (see Fig. 4Snapshots of the deuterium jet and droplets. From left to right, frames are separated by 33.3 μs. The red line indicates the trajectory of one single droplet and allows for measuring the droplet and jet velocity ($v_J \approx 4.4\,\mathrm{m/s}$). The blue area indicates the region near the breakup. The red area indicates the furthest regionfigure.4). Each droplet being in the wake of the preceding droplet, it experiences a negligible drag and thus keeps its initial velocity equal to the velocity of the jet v_J. The explored range of pressure differences between the deuterium reservoir and the helium cryostat is 60-89 mbar. In those conditions, v_J ranges between 4 m/s and 12 m/s, which is much larger than the expected settling velocity v_s of an isolated droplet. The latter is given, for deuterium particles in quiescent helium, by

$$v_s = \frac{D^2 g}{18\nu}\left(\frac{\rho_{D_2}}{\rho_{He}} - 1\right), \tag{1}$$

where ν is the kinematic viscosity of helium. Assuming the surrounding helium is at 10 K, $v_s \approx 0.1\,\mathrm{m/s}$.

The inter-droplet distance immediately downstream of the jet breakup is an indirect measure of the droplet production frequency. The distribution of these distances, shown in Fig. 5Distribution of the inter-droplet distancefigure.5, is characterized by a mean distance $\langle\delta\rangle \approx 4.4D_N$ and a standard deviation $\sigma_\delta \approx 1.6D_N$, in agreement with the wavelength of the instability observed directly on the jet in Fig. 3Destabilization and fragmentation of the deuterium jetfigure.3. This observation is the signature of the Rayleigh-Plateau instability (see Refs. [36–39]) whose most unstable mode is characterized by a wavelength $\lambda_{max} = \pi/0.607D_N \approx 4.5D_N$.

The apparent area A of the droplets is measured and their diameter D and volume V are deduced by assuming the sphericity of the droplets $D = 2(A/\pi)^{1/2}$ and $V = \frac{4\pi}{3}(A/\pi)^{3/2}$. The distribution of droplet diameters is shown in Fig. 6Distribution of droplet adimensionalized volume (main figure) and diameter (insert). The distributions are computed over 17500 particles in the region near the breakup (blue) and 12500 particles in the lowest visualized region (red) (see Fig. 4Snapshots of the deuterium jet and droplets. From left to right, frames are separated by 33.3 μs. The red line indicates the

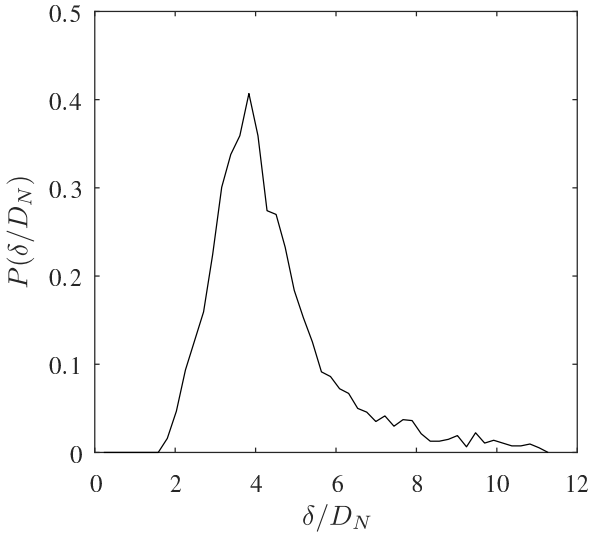

FIG. 5. Distribution of the inter-droplet distance

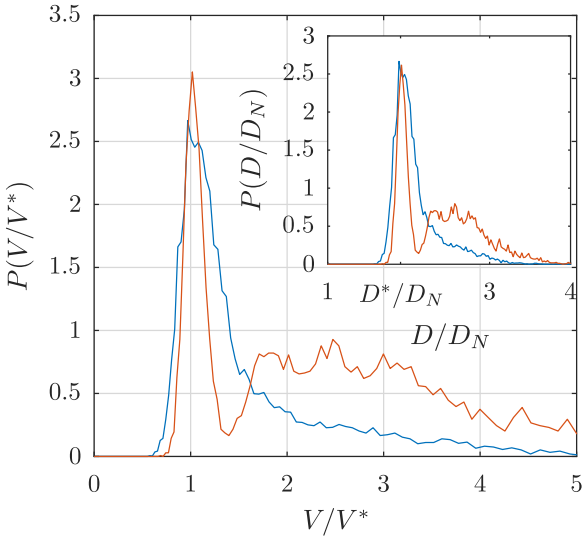

FIG. 6. Distribution of droplet adimensionalized volume (main figure) and diameter (insert). The distributions are computed over 17500 particles in the region near the breakup (blue) and 12500 particles in the lowest visualized region (red) (see Fig. 4Snapshots of the deuterium jet and droplets. From left to right, frames are separated by 33.3 μs. The red line indicates the trajectory of one single droplet and allows for measuring the droplet and jet velocity ($v_J \approx 4.4\,\mathrm{m/s}$). The blue area indicates the region near the breakup. The red area indicates the furthest regionfigure.4). As the jet direction is not strictly aligned with the camera focal plane, droplets far from the nozzle are slightly out of focus. The calibration of the lowest zone is thus adjusted so that the volume of single droplets in higher and lowest zone coincide

trajectory of one single droplet and allows for measuring the droplet and jet velocity ($v_J \approx 4.4\,\mathrm{m/s}$). The blue area indicates the region near the breakup. The red area indicates the furthest regionfigure.4). As the jet direction is not strictly aligned with the camera focal plane, droplets far from the nozzle are slightly out of focus. The calibration of the lowest zone is thus adjusted so that the volume of single droplets in higher and lowest zone coincidefigure.6. The most probable diameter $D^* \approx 1.9D_N$ is in agreement with the Rayleigh-Plateau instability mechanism mentioned above. The overall diameter distribution is $D = 2 \pm 0.25D_N$. The distribution of droplet volumes is also shown in Fig. 6Distribution of droplet adimensionalized volume (main figure) and diameter (insert). The distributions are computed over 17500 particles in the region near the breakup (blue) and 12500 particles in the lowest visualized region (red) (see Fig. 4Snapshots of the deuterium jet and droplets. From left to right, frames are separated by 33.3 μs. The red line indicates the trajectory of one single droplet and allows for measuring the droplet and jet velocity ($v_J \approx 4.4\,\mathrm{m/s}$). The blue area indicates the region near the breakup. The red area indicates the furthest regionfigure.4). As the jet direction is not strictly aligned with the camera focal plane, droplets far from the nozzle are slightly out of focus. The calibration of the lowest zone is thus adjusted so that the volume of single droplets in higher and lowest zone coincidefigure.6 adimensionalized by the most probable volume $V^* = \pi D^{*3}/6$. Immediately after the jet breakup the droplets have an average volume $V \approx 1 \pm 0.2V^*$.

At the lowest point of our field of view (at a distance $2 \rightarrow 3\,\mathrm{mm}$ or $100 \rightarrow 200D_N$ downstream the jet breakup), the volume distribution is polydisperse, with the presence of larger droplets (see Fig. 6Distribution of droplet adimensionalized volume (main figure) and diameter (insert). The distributions are computed over 17500 particles in the region near the breakup (blue) and 12500 particles in the lowest visualized region (red) (see Fig. 4Snapshots of the deuterium jet and droplets. From left to right, frames are separated by 33.3 μs. The red line indicates the trajectory of one single droplet and allows for measuring the droplet and jet velocity ($v_J \approx 4.4\,\mathrm{m/s}$). The blue area indicates the region near the breakup. The red area indicates the furthest regionfigure.4). As the jet direction is not strictly aligned with the camera focal plane, droplets far from the nozzle are slightly out of focus. The calibration of the lowest zone is thus adjusted so that the volume of single droplets in higher and lowest zone coincidefigure.6). These droplets result from the coalescence of 2, 3, or more rarely 4 initial droplets. In this observation area, about 1/3 of the droplets are the result of such a process. At this stage, this coalescence phenomenon concerns about 50 % of the initially formed droplets. It is made possible by the fact that the ejection speed of the droplets is slightly distributed: to erase the initial separation distance ($4.5D_N$) over a distance of $100D_N$, a velocity difference of 4.5 % is sufficient. This gives an order of magnitude of the width of the velocity distribution of the droplets.

The collection of droplets (and therefore of tracers) finally obtained is therefore not strictly monodisperse. However, the diameter distribution remains reasonably narrow: the maximum observed volume for the droplets corresponds to the coalescence of 4 initial droplets, which corresponds to an increase in the initial diameter of 60 % only.

B. Drop-on-demand

In the drop-on-demand mode, the pressure difference that is necessary to make the liquid flow out of the nozzle is supplied by periodic *water hammer* like pressure pulses. Actually, the average pressure difference between the liquid deuterium reservoir and the helium cryostat has to be much smaller than in continuous mode, and was maintained at $\Delta P = 5\,\mathrm{mbar}$.

The pressure pulses are obtained thanks the 30 mm long glass duct upstream the nozzle that is encapsulated in a piezo-transducer. Driving the transducer with suitable voltage pulses (see the example in Fig. 7Typical shape of the driving voltage for the piezo-transducerfigure.7), one can modulate the diameter of the tube and create the above mentioned water hammer like pressure increases at the nozzle, leading to the detachment of liquid droplets.

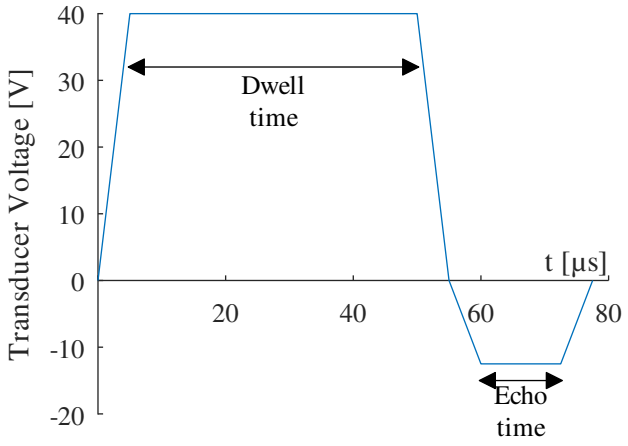

FIG. 7. Typical shape of the driving voltage for the piezo-transducer.

Depending on the excitation parameters each pulse produces either a single dropplet or a pair of dropplets: the main one and a so called satelite which is smaller, and ejected in a different direction than the former.

Due to the different ejection directions, coalescence of droplets is much less probable than in the continuous jetting settup. Nevertheless, we could clearly observe such droplet coalescence of fast main droplets with slow satellites. This shows that no complete freezing happens in the observation area, at least for the fastest particles.

Due to the finite depth of field of our setup, the apparent area of droplets varies continuously along the measurement region. In absence a robust criterion to decide where the droplet is in focus, we chose to measure the mean diameter and its standard deviation in the 1 mm long region where the area is minimum. With this criterion the diameter of the main droplet has a diameter $D/D_N \approx 2.1 \pm 0.03$, independent of the presence of a satellite (see Fig. 8Distribution of droplet diameter computed over an average of 106 particles for the five drop-on-demand runs: 1 (blue), 2 (red), 3 (yellow), 4 (purple) and 5 (green). Solid lines correspond to main droplets while dashed lines correspond to satellitesfigure.8).

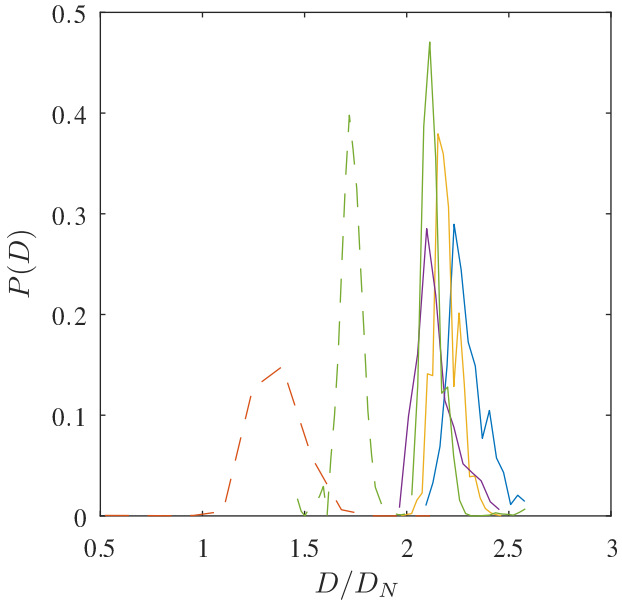

FIG. 8. Distribution of droplet diameter computed over an average of 106 particles for the five drop-on-demand runs: 1 (blue), 2 (red), 3 (yellow), 4 (purple) and 5 (green). Solid lines correspond to main droplets while dashed lines correspond to satellites.

TABLE I. Summary of droplet characteristics in drop-on-demand setup. The diameter D and its standard deviation D are measured over a 1 mm region where the apparent droplet area is minimum. The initial velocity v_0 is computed at the beginning of valid tracks.

N	**Main**		**Satellite**	
	D/D_N	v_0 [m/s]	D/D_N	v_0 [m/s]
1	2.2 ± 0.02	1.7	-	-
2	-	-	1.4 ± 0.18	0.2
3	2.2 ± 0.07	1.1	-	-
4	2.1 ± 0.02	1	-	-
5	2.1 ± 0.03	1.8	1.7 ± 0.04	0.8

The latter, when present, has a smaller diameter and velocity. The observed values for the mean diameter, its dispersion, and the initial droplet velocity are summarized in table ISummary of droplet characteristics in drop-on-demand setup. The diameter D and its standard deviation D are measured over a 1 mm region where the apparent droplet area is minimum. The initial velocity v_0 is computed at the beginning of valid trackstable.1.

Contrary to the continuous jet setup, the distance between the droplets is large, of the order of tens of droplet diameters, and the surrounding helium can be considered at rest. One of the consequences if that the droplet velocity decreases much more rapidly than in continuous mode. The settling velocity, $v_s \approx 0.1\,\mathrm{m/s}$ at $T = 15\,\mathrm{K}$, is reached in the field of view for the slowest droplets. For the fastest droplets, we could verify that approximating their velocity by integrating the equation

of motion

$$v(t) = v_0 + \int_0^t dt' \left[(1 - \rho_{He}/\rho_{D_2})\, g - Cx \frac{3\rho_{He}}{4\rho_{D_2} D} v(t')^2 \right], \quad (2)$$

where $Cx \approx 24/Re \times (1 + 0.15Re)^{0.687}$ is the drag coefficent for a sphere at low to moderate Reynolds number[40], $Re = Dv/\nu$, gives very good agreement and that they reached the terminal velocity at a maximum distance from the nozzle of about 6 mm.

V. POST EVOLUTION AND FREEZING

Inside the field of view we observe the coalescence of the deuterium droplets, which shows that they are in a liquid state.

In order to determine the future evolution of these droplets, we propose below a rough model of the heat exchange they undergo, in order to estimate an order of magnitude of their freezing time. This estimation is particularly difficult, as the temperature field in the helium atmosphere is not well known: near the helium liquid bath surface, it is equal to the saturation temperature ($T = 4.2\,\mathrm{K}$), while near the injector, it is thermally influenced by the nozzle heater (probably close to 15-20 K).

The heat exchange undergone by the droplets is the result of two contributions: (i) the heat convection flux φ_{conv}, due to the temperature difference between the surface of the droplets (at T_{surf}) and the helium atmosphere (at T_{He}), and (ii) the evaporation φ_{evap} due to the deuterium concentration gradient. If we assume that the typical distance over which both the temperature and concentration gradients are established is of the order the drop radius $R_d = 20\,\mu\mathrm{m}$, we can give a rough estimate of both terms. The convection term can be written:

$$\varphi_{conv} \sim \frac{k(T_{surf} - T_{He})}{R_d} \approx 16\,\mathrm{kW/m^2}, \quad (3)$$

with $T_{He} = 4.2\,\mathrm{K}$, $T_{surf} = 20\,\mathrm{K}$, and $k \approx 0.02\,\mathrm{W/K}$ (obtained from Hepak® library) is the thermal conductivity of helium at an intermediate temperature $T = 12\,\mathrm{K}$. The heat flux associated with the evaporation of liquid deuterium is given by Fick's law for mass diffusion, due to deuterium concentration gradients, multiplied by the evaporation enthalpy. Given that the partial pressure of deuterium at the surface of the droplet is the saturation pressure, $P_{sat} = 0.17\,\mathrm{bar}$, and assuming that it becomes negligible a few radius R_d away, one can write the associated heat flux:

$$\varphi_{evap} \sim \Delta H_{vap} \frac{D_{D_2/He} M P_{sat}}{R_d R_i T_{surf}} \approx 21\,\mathrm{kW/m^2}, \quad (4)$$

with $\Delta H_{vap} = 320\,\mathrm{kJ/kg}$ the latent heat of vaporization, $D_{D_2/He} \approx 1.5 \times 10^{-6}\,\mathrm{m^2/s}$ the diffusion coefficient of deuterium vapor in helium (assumed to be equal to the kinematic viscosity of helium obtained from Hepak® library), $M = 4\,\mathrm{g/mol}$ the molecular mass of deuterium and R_i the perfect gas constant.

For an accurate estimation, a distinction must be made between the behavior of droplets resulting from jet breakage by the Rayleigh-Plateau mechanism, and those resulting from the drop-on-demand process. As shown by the analysis of their trajectory, the former are in the wake of each other (their displacement is at constant speed). Their wake is then at a temperature close to the temperature of the droplets, and the concentration of deuterium vapor close to saturation. The effective exchange surface S for a droplet is thus that of a cylinder of radius R_d and height $\delta \sim 4.5 D_N \sim 4.5 R_d$, and does not differ significantly from the surface of the droplets. For the drop-on-demand case, the droplets can be considered as isolated. Moreover, their velocity is low ($Re \sim 20$) so that convection effects do not modify the orders of magnitude.

Neglecting sensitive heat (Stefan number is $Ste = C\Delta T/\Delta H_{sol} \approx 0.16$ with $\Delta T = T_{init} - T_{sol} = 2\,\mathrm{K}$, $\Delta H_{sol} \approx 49\,\mathrm{kJ/kg}$ and $C \approx 4\,\mathrm{kJ/kg}$, see Souers[41]), we expect the droplets to freeze in a time of the order of

$$\tau = \frac{m_d \Delta H_{sol}}{4\pi R_d^2 (\varphi_{cond} + \varphi_{evap})} \sim 1.5\,\mathrm{ms}. \quad (5)$$

For this estimate of the freezing time to be relevant, we must ensure that the heat has time to leave the drop by diffusion from its core to its surface. The thermal diffusion time is given by $\tau_{diff} = R_d^2/4D_{th} = 0.7\,\mathrm{ms}$, where $D_{th} \approx 1.4 \times 10^{-7}\,\mathrm{m^2/s}$ designates the thermal diffusivity in liquid deuterium. Although not negligible, this time is effectively shorter than the freezing time, which ensures that the drop freezes en masse. Due to the strong temperature dependence of the exchange coefficients of gas helium, the exchanges are overestimated (by a factor not exceeding 2). In the absence of a better knowledge of the conditions, we therefore remain with these estimates.

For droplets formed from a continuous jet (Rayleigh-Plateau fragmentation), we expect droplet freezing to occur at a distance of about 6 to 18 mm from the nozzle (i.e. 2 – 4 times the height of the field of view). The droplet coalescence processes observed in the viewing area are therefore likely to occur again. However, due to the conservation of the global momentum, the velocity of the coalesced droplets is the average of the velocities of the droplets that form it. It is therefore less widely distributed. The inter-droplet distances are increased in proportion to the coalescence number. The evolution of the volume distribution of the droplets should therefore be limited and our observations should be representative of the final sizes of the tracers.

For the drop-on-demand experiments, the time of presence of the droplets in the viewing area is comparable to the estimated freezing time. The observation of the absence of freezing does not contradict our estimates, as a higher temperature of the helium vapours near the nozzle is expected.

In any event, if the injection nozzle is placed at a reasonable distance from the liquid helium free surface, say 10 cm, the travel time to reach the free surface (of order 1 s here) is expected to be much larger than the above estimations for freezing time. We thus expect that the droplets will freeze well before impinging the free surface and that droplets should retain their initial spherical geometry with a slightly smaller diameter: The density of solid deuterium being about 13% larger

(see Souers[41]), the resulting particle diameter is expected to be 4.5% smaller.

VI. CONCLUSIONS AND FURTHER REMARKS

In this section we first recall the main features of the two particle seeding techniques that we have described in this article. We then discuss their respective advantages, limitations and application field.

A. Diameters distribution

The Rayleigh-Plateau fragmentation produces particles with overall diameters $D = 2 \pm 0.25 D_N$. The quite large width of the distribution is essentially due to the coalescence of droplets with different velocities and this situation could actually be improved. In the current setup, the fragmentation frequency, and thus the width of the diameter distribution, is driven by the instability only. In order to improve the diameter distribution, we plan on using the piezo-actuator to prescribe the fragmentation frequency (see e.g. Refs. [32 and 34]). The expected effect of this strategy is twofold: (i) narrow down the size distribution of primary droplets and (ii) homogenize the particle velocities so that probability of particle collision gets smaller.

The drop-on-demand setup produces droplets with narrower diameter distributions of order $D \approx 2.1 \pm 0.05 D_N$. Tunning the parameters of the piezo-actuator to produce single droplets (without satelite) is not an easy task though and the careful study of all those parameters is still work in progress.

In both cases the resulting particles diameter, of the order of 40 µm, is higher than that reported for gas flakes, in the range 3-10 µm (see, e.g., La Mantia and Skrbek[42]). Note though that the latter estimation is based on the assumption of sphericity and compacity, which has never been proven to the best of our knowledge.

Reaching smaller particle diameters, say 10 µm, with our setup, would require using nozzles of diameter $D_N = 5\,\mu$m. In order to retrieve the same Rayleigh-Plateau regime, we would have to make sure to stay in the same range of Weber numbers,

$$We = \rho_{D_2} v_n^2 D_N / \sigma, \tag{6}$$

where $\sigma \approx 3.8\,$mN/m is the surface tension. This would involve increasing the nozzle velocity v_n by a factor of 2, leading to a pressure loss 32 times larger, still manageable. As for the drop-on-demand regime, the provider does not officially supply nozzle diameters lower than 20 µm but can reduce the diameter on special request down to $D_N = 5\,\mu$m.

B. Particle production rate

The particle production rate for the Rayleigh-Plateau setup is essentially given by the jet velocity. The latter must be high enough to avoid dripping and low enough to not enter the first wind regime, where the influence of the surrounding gas flow becomes important. The transition from dripping to Rayleigh-Plateau (or jetting) regime is usually assumed to happen when the liquid Weber number exceeds a critical value of order $We_c = 8$ (see Ref. 43). In the jetting regime the inter droplet distance is fixed $\lambda \approx 9/2 D_N$, and the smallest achievable droplet production rate $\dot{n}$ is thus given by

$$\dot{n} = \frac{2}{9}\sqrt{\frac{We_c \sigma}{\rho_l D_N^3}}. \tag{7}$$

For liquid D_2 through a 20 µm orifice, the minimum frequency is thus of the order of $\dot{n} \approx 33\,$kHz and this frequency increases as the orifice diameter decreases.

In comparison, the production rate of the drop-on-demand setup is much lower: In our experiments we did not exceed $\dot{n} = 500\,$Hz but the device is theoretically designed to allow rates up to $\dot{n} = 2\,$kHz.

C. Particles as tracers

The produced solid particles are intended to seed a flow of liquid helium and, ideally, to remain attached to a fluid particle. In a turbulent flow, spacial velocity fluctuations occurs on very small scales, down to η the Kolmogorov scale. For typical liquid helium turbulence experiments η is smaller than $50\,\mu$m, so that the particles described in the present paper fail to completely describe the smallest structures of most turbulent flows. However, commercially available hollow glass spheres with density matching that of liquid helium exceed 80 µm because of their finite thickness. Our particles are then better candidates. Producing smaller in size particles by simply choosing a smaller nozzle diameter will solve this issue.

The inertia of the particles is characterized by the particle velocity adaptation time $\tau_P = \frac{D^2}{36}\frac{\rho_P + \rho_f}{\mu}$. For the 40 µm particles we produced, this time is of the order of $\tau_P \approx 3\,$ms. This time should be compared with the characteristic time of velocity fluctuations at the particle scale ($\tau_D = \tau_L (D/L)^{2/3}$ as $D \gtrsim \eta$). For typical liquid helium turbulence τ_D ranges from 2 ms to 10 ms for experiments conducted in metric vessels at high velocity[1]. This leads to stokes numbers of order unity, of the same order of magnitude as those computed by Outrata *et al.*[44] for 30 µm deuterium particles, and the requirement for a small inertia is thus nearly satisfied by our particles and this would be even more true for smaller particles.

Finally, the density of deuterium particles is slightly higher than that of liquid helium. They are therefore likely to sediment or more generally to not follow the streamlines of the flow and be attracted to areas of high pressure. The particles thus formed are therefore not perfect tracers of liquid helium flows. Note that both the settling velocity [eq. (1equation.4.1)] and the Stokes number are proportional to the square of the diameter, and that obviously decreasing the particle diameters will make those issues negligible. Moreover, it is possible to replace the deuterium with hydrogen deuteride (see, e.g., Švančara *et al.*[8]). The resulting particles density will match nearly perfectly that of liquid helium.

VII. ACKNOWLEDGMENTS

This work was supported by CEA Bottom-Up Exploratory Programme (grant 21P44 MDET).

VIII. DATA AVAILABILITY

The data that support the findings of this study are available from the corresponding author upon reasonable request.

[1] J. Salort, F. Chillà, E. Rusaouën, P.-E. Roche, M. Gibert, I. Moukharski, A. Braslau, F. Daviaud, B. Gallet, E.-W. Saw, B. Dubrulle, P. Diribarne, B. Rousset, M. B. Mardion, J.-P. Moro, A. Girard, C. Baudet, V. L'vov, A. Golov, and S. Nazarenko, New J. Phys. **23**, 063005 (2021).
[2] L. Tisza, Nature **141**, 913 (1938).
[3] L. Landau, Phys. Rev. **60**, 356 (1941).
[4] S. Babuin, E. Varga, L. Skrbek, E. Lévêque, and P.-E. Roche, Europhysics Letters **106**, 24006 (2014).
[5] Y. Tang, W. Guo, V. S. L'vov, and A. Pomyalov, Phys. Rev. B **103**, 144506 (2021).
[6] J. Tough (Elsevier, 1982) pp. 133–219.
[7] P. Švančara and M. La Mantia, Journal of Fluid Mechanics **876**, R2 (2019).
[8] P. Švančara, P. Hrubcová, M. Rotter, and M. La Mantia, Phys. Rev. Fluids **3**, 114701 (2018).
[9] D. Durì, C. Baudet, J.-P. Moro, P.-E. Roche, and P. Diribarne, Reviews of Scientific Instruments **86**, 025007 (2015).
[10] P. Diribarne, B. Rousset, Y. A. Sergeev, J. Valentin, and P.-E. Roche, Phys. Rev. B **103**, 144509 (2021), publisher: American Physical Society.
[11] P. Diribarne, M. Bon Mardion, A. Girard, J.-P. Moro, B. Rousset, F. Chilla, J. Salort, A. Braslau, F. Daviaud, B. Dubrulle, B. Gallet, I. Moukharski, E.-W. Saw, C. Baudet, M. Gibert, P.-E. Roche, E. Rusaouen, A. Golov, V. L'vov, and S. Nazarenko, Phys. Rev. Fluids **6**, 094601 (2021).
[12] J. Salort, A. Monfardini, and P.-E. Roche, Review of Scientific Instruments **83**, 125002 (2012).
[13] E. Woillez, J. Valentin, and P.-E. Roche, Europhysics Letters **134**, 46002 (2021).
[14] T. Zhang and S. W. Van Sciver, Journal of Low Temperature Physics **138**, 865 (2005).
[15] B. Mastracci, S. Bao, W. Guo, and W. F. Vinen, Phys. Rev. Fluids **4**, 083305 (2019).
[16] P. Švančara, D. Duda, P. Hrubcová, M. Rotter, L. Skrbek, M. La Mantia, E. Durozoy, P. Diribarne, B. Rousset, M. Bourgoin, and et al., Journal of Fluid Mechanics **911**, A8 (2021).
[17] M. Gibert, C. Peretti, J. Vessaire, and E. Durozoy, "Direct visualization of the quantum vortex density law in rotating 4he," (2022), arXiv:2212.12250 [cond-mat.other].
[18] G. P. Bewley, M. S. Paoletti, K. R. Sreenivasan, and D. P. Lathrop, Proceedings of the National Academy of Sciences **105**, 13707 (2008).
[19] S. Yui, H. Kobayashi, M. Tsubota, and W. Guo, Phys. Rev. Lett. **124**, 155301 (2020).
[20] U. Giuriato and G. Krstulovic, Scientific Reports **9**, 4839 (2019).
[21] J. I. Polanco and G. Krstulovic, Phys. Rev. Fluids **5**, 032601 (2020).
[22] T. Zhang, D. Celik, and S. W. Van Sciver, Journal of Low Temperature Physics **134**, 985 (2004).
[23] F. Bielert and G. Stamm, Cryogenics **33**, 938 (1993).
[24] D. Çelik, M. R. Smith, and S. W. Van Sciver, "A particle seeding apparatus for cryogenic flow visualization," in *Advances in Cryogenic Engineering*, edited by Q.-S. Shu (Springer US, Boston, MA, 2000) pp. 1175–1180.
[25] F. Sy, P. Diribarne, B. Rousset, M. Gibert, and M. Bourgoin, Phys. Rev. Fluids **6**, 064604 (2021).
[26] E. J. Yarmchuk, M. J. V. Gordon, and R. E. Packard, Phys. Rev. Lett. **43**, 214 (1979).
[27] W. Guo, D. Jin, G. M. Seidel, and H. J. Maris, Phys. Rev. B **79**, 054515 (2009).
[28] D. P. Meichle and D. P. Lathrop, Review of Scientific Instruments **85** (2014), 10.1063/1.4886811, 073705.
[29] W. Guo, M. La Mantia, D. P. Lathrop, and S. W. Van Sciver, Proceedings of the National Academy of Sciences **111**, 4653 (2014).
[30] W. Guo, Journal of Low Temperature Physics **196**, 60 (2019).
[31] D. Celik and S. Van Sciver, Experimental Thermal and Fluid Science **26**, 971 (2002).
[32] A. V. Boukharov, M. Büscher, A. S. Gerasimov, V. D. Chernetsky, P. V. Fedorets, I. N. Maryshev, A. A. Semenov, and A. F. Ginevskii, Phys. Rev. Lett. **100**, 174505 (2008).
[33] A. V. Boukharov, A. F. Ginevsky, and E. V. Vishnevsky, Journal of Physics: Conference Series **1565**, 012029 (2020).
[34] R. A. C. Fraga, A. Kalinin, M. Kühnel, D. C. Hochhaus, A. Schottelius, J. Polz, M. C. Kaluza, P. Neumayer, and R. E. Grisenti, Review of Scientific Instruments **83** (2012), 025102.
[35] I. H. Bell, J. Wronski, S. Quoilin, and V. Lemort, Industrial & Engineering Chemistry Research **53**, 2498 (2014).
[36] J. A. F. Plateau, *Statique expérimentale et théorique des liquides soumis aux seules forces moléculaires*, Vol. 2 (Gauthier-Villars, 1873).
[37] L. Rayleigh, The London, Edinburgh, and Dublin Philosophical Magazine and Journal of Science **34**, 177 (1892).
[38] S. Chandrasekhar, *Hydrodynamic and hydromagnetic stability* (Oxford University Press, 1961).
[39] D. B. Bogy, Annual Review of Fluid Mechanics **11**, 207 (1979).
[40] V. L. Schiller, Z. Vereines Deutscher Inge. **77**, 318 (1933).
[41] P. C. Souers, *Hydrogen Properties for Fusion Energy* (University of California Press, Berkeley, 1986).
[42] M. La Mantia and L. Skrbek, Europhysics Letters **105**, 46002 (2014).
[43] W. E. Ranz, *On sprays and spraying: A survey of spray technology for research and development engineers*, 65 (Literary Licensing, LLC, 1956).
[44] O. Outrata, M. Pavelka, J. Hron, M. La Mantia, J. Polanco, and G. Krstulovic, Journal of Fluid Mechanics **924**, A44 (2021).